Multimodal microscopy of extended defects in β-Ga_2O_3 (010) EFG crystals

Cite as: AIP Advances 13, 075122 (2023); doi: 10.1063/5.0158904
Submitted: 18 May 2023 • Accepted: 3 July 2023 •
Published Online: 18 July 2023

Drew Haven,[1] Helio Moutinho,[2] John S. Mangum,[2] Harvey Guthrey,[2] David Joyce,[1] Andriy Zakutayev,[2] and Nancy M. Haegel[2,a)]

AFFILIATIONS

[1] Luxium Solutions LLC, Milford, New Hampshire 03055, USA
[2] National Renewable Energy Laboratory, Golden, Colorado 80401, USA

[a)] Author to whom correspondence should be addressed: nancy.haegel@nrel.gov

ABSTRACT

Beta-phase gallium oxide (β-Ga_2O_3) has attracted attention in recent years as a potentially low cost, large area substrate and active layer material for high power, high temperature power electronics and sensing devices. However, growth of β-Ga_2O_3 crystals is complicated by easily activated (100) and (001) cleavage planes, the presence of low angle grain boundaries (LAGBs) and twins, and the potential formation of polycrystalline grains. In this study, β-Ga_2O_3 crystals were grown by the edge-defined film-fed growth technique with an (010) principal face. Two crystals with apparently randomly formed high angle grain boundaries (HAGBs) were selected and analyzed by electron backscatter diffraction, electron channeling contrast imaging, and cathodoluminescence to investigate the nature of the LAGBs and the source of the HAGB formation. It was discovered that planar LAGBs lying parallel to the (010) plane exist in the region immediately preceding the start of an HAGB. Increased misorientation across the LAGB was observed, approaching the initiation of a new grain. We present multimodal microscopy characterization, correlating misorientation and variation in optoelectronic properties with LAGBs and the associated dislocations.

Interest in gallium oxide as a next generation power electronics and high temperature sensing material is driven by its wide bandgap and high critical electric field strength, coupled with the possibility of potentially low cost manufacturing for large area bulk substrates. The latter is dependent on scalable growth techniques from a melt, such as Edge-defined Film-fed Growth (EFG) or Czochralski (CZ) methods. The pathway to scalable substrate manufacturing makes this ultrawide bandgap (UWBG) semiconductor material currently unique. As the size and quality of the substrates increase, it becomes increasingly important to understand the nature and impact of extended defects that arise and propagate during bulk growth. A recent review article identified six challenges for EFG and CZ crystal growth of Ga_2O_3.[1] Four of these—scalability, yield, defect mitigation, and crystalline uniformity—depend on understanding and controlling bulk defects such as twins, grain boundaries, and dislocations.

EFG has potential advantages for bulk growth of Ga_2O_3 in terms of both cost and scaling, as indicated in a recent technoeconomic analysis.[2] With regard to scaling of bulk crystal size, the relatively low thermal conductivity of gallium oxide is a limiting factor for three dimensional growth, with thermal stresses limiting the boule diameter. Since EFG scales largely two dimensionally (width and length), it does not suffer from limitations related to thermal conductivity in the same way as other bulk growth methods do. For example, the CZ growth of Al_2O_3 is limited to 4–5 in. diameter, whereas commercially-grown EFG sapphire can reach areal sizes of 12 × 26 in.^{2} and larger. Although the grown volumes are similar, the achievable areas are significantly different.

There has been extensive work on the understanding and characterization of point defects in Ga_2O_3.[3,4] Significantly less work has been carried out, however, on the nature of extended defects, their role in bulk crystal growth, and the resulting correlation of structural and electronic properties. Ueda *et al.* provided a recent review of the extended defects and classified them into four types—dislocations, stacking faults, twins, and nanovoids—which were studied by etching, x-ray diffraction, and TEM.[5] While information on the

structural nature of these defects, associated slip systems, and possible generation mechanisms has been emerging, further work is required to understand their origin, propagation during crystal growth, and potential impact on device properties.

We present a multiscale, multimodal study of an unusual planar defect generated during EFG synthesis of (010) beta-phase gallium oxide (β-Ga_2O_3) ribbons, whose principal surface is the (010) plane. This defect is a low angle grain boundary (LAGB) associated with the generation of a high angle grain boundary (HAGB) as it propagates in the growth direction. Increasing angular mismatch across the grain boundary as it propagates in the growth direction is demonstrated using electron backscatter diffraction (EBSD). LAGBs in this material are further characterized by electron channeling contrast imaging (ECCI) and cathodoluminescence (CL), bringing this collection of microscopic characterization tools together for the first time in EFG Ga_2O_3 to provide insight into defect behavior and propagation during bulk growth.

For this study, several β-Ga_2O_3 crystals, known as ribbons, were grown by the EFG technique. All were grown with a (010) principal face, pulled in the [001] direction, and were iron (Fe)-doped to a target concentration of ~6×10^{18} cm^{-3}, resulting in high resistivity material. The raw materials used were high purity powders of gallium oxide (Ga_2O_3, 99.999%) and iron oxide (Fe_2O_3, 99.99%). The crystals were grown using an iridium crucible and die (Fig. 1) in an RF induction furnace operating at 10 kHz, in an atmosphere of mixed oxygen and argon. The die was 2 mm thick and 25 mm wide, resulting in ribbons of ~$2 \times 25 \times 50$ mm^3. Raw materials were heated to melt over the course of ~4 h, and a crystal was grown using a single crystal gallium oxide seed to a length of ~50 mm.

We applied three techniques that leverage characterization capabilities in a scanning electron microscope (SEM)—EBSD, ECCI, and CL—to provide multiscale, multimodal characterization of structural defects. Electron beam imaging in the SEM is well suited to range from the millimeter to submicrometer scale. Identification of specific regions, whether through focused ion beam (FIB) marks on the surface or use of characteristic topography, can allow the same location to be identified and imaged at different times and using different microscopes. These SEM-based techniques require less specialized sample preparation than the TEM and can also identify regions for further high-resolution investigation.

EBSD[6,7] uses the electron beam, incident upon the sample of interest, to generate diffracted electrons. By scanning the beam over the sample and analyzing the resulting Kikuchi patterns, a map with the orientation of the sample surface is generated. EBSD analysis was performed in a ThermoFisher NanoSEM Nova 630 using Oxford Instruments AZtecHKL with a symmetry detector. The analysis was performed with the sample tilted at 70° to increase the yield of diffracted electrons, which can cause surface topography to absorb some diffracted electrons, resulting in an effect known as shadowing.[8] To minimize this issue, some samples were ion milled in JEOL cross section ion milling systems IB-09010CP or IB-19520CCP.

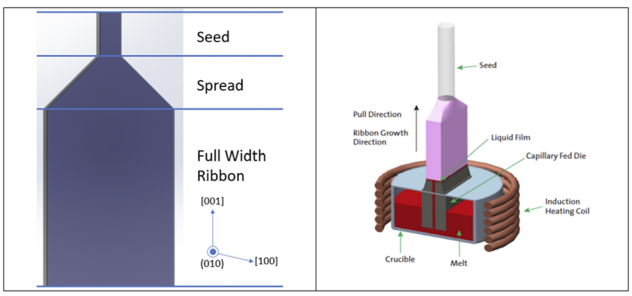

FIG. 1. Schematics of EFG crystal growth components and an example ribbon, indicating definition and locations of seed, spread, and full width ribbon. The crystals are pulled in the [001] direction.

The angular resolution of standard EBSD is ~0.05°, which makes the technique suitable for studying low-angle grain boundaries. EBSD can provide a wide range of information, including local strain[9] and the degree of misorientation between pixels or across boundaries. In this work, we present inverse-pole-figure (IPF) and orientation spread maps.

EBSD characterization for Ga_2O_3 has been applied primarily for orientation mapping and spatial identification of the location of extended defects. Jesenovec *et al.* used EBSD of Zn-doped β-Ga_2O_3 Czochralski single crystals to identify the surface orientation for electrical and optical measurements.[10] Golz *et al.* utilized high resolution EBSD to locate grain boundaries in CZ-grown Ga_2O_3, enabling study of the effect of grain boundaries on the electrical conductivity tensor.[11] EBSD was also used by Oshima *et al.* to identify the in-plane orientation for κ-Ga_2O_3 islands and structures created by epitaxial lateral overgrowth on sapphire substrates.[12]

ECCI is an SEM-based technique for imaging lattice defects and strain fields in crystalline materials.[13] Any crystalline defect or strain that disrupts the periodic lattice, and therefore electron channeling conditions, will locally enhance the number of backscattered electrons and cause increased image contrast in the vicinity of the defect. ECCI has been used to locate and quantify crystalline defects in a variety of materials, including group IV and III-V semiconductors, nitrides, and metals.[14–16] Picard[17] showed an array of dislocations on a Ga_2O_3 (−201) bulk crystal surface, but broad application of ECCI in Ga_2O_3 appears limited. The technique has been identified, however, as having significant potential for UWBG materials as a part of multimodal characterization.[18]

ECCI was performed using a retractable backscatter detector inserted underneath the polepiece on either an FEI Nova NanoSEM 630 SEM operating at 25 kV accelerating voltage and 3.2 nA beam current or a TESCAN Amber S8252G SEM operating at 30 kV accelerating voltage and 10 nA beam current. The channeling conditions were set up by orienting the electron beam axis at the edge of either Ga_2O_3 (010) or (200) Kikuchi bands and are indicated in the figures.

Cathodoluminescence involves the generation and spatially and spectrally resolved collection of luminescence from an incident electron beam. For semiconductors, this emission can come from band to band recombination, defect related recombination, or internal transitions associated with certain elements (e.g., rare earth elements such as Er in Si). CL has been used extensively in the characterization of Ga_2O_3 since the electron beam provides excitation for both band to band and defect recombination.[3] CL spectrum imaging was performed at room temperature in a JEOL JSM 7600 FESEM equipped with a Horiba H-CLUE CL system. The SEM beam conditions were 15 kV accelerating voltage and ~3 nA current, chosen to maximize a balance of signal and spatial resolution.

Spectrum-per-pixel data collection was accomplished using a parabolic light-collection mirror and an iHR320 spectrometer equipped with a thermoelectrically cooled Si charge-coupled device (CCD). Spectrum imaging data were then processed to produce integrated intensity images.

Characterization of the EFG material was motivated by the desire to understand the formation of HAGBs in such particular melt-grown β-Ga_2O_3. Typically, development of HAGBs in seeded bulk growth methods follows a common breakdown pattern. High levels of dislocations begin to coalesce to form LAGBs; then when angular mismatch of the LAGBs becomes too high, an HAGB is formed to relieve the associated strain. This breakdown can almost always be traced by the unaided eye as the formation and development of LAGBs take place over mm to cm scales. However, this was not observed on the grown ribbons even under microscopic examination.

Samples for the study were taken from two ribbons that had a HAGB in the spread region of growth (Fig. 2). The regions taken for analysis were prepared by cleaving on the (100) and (001) planes from locations immediately preceding the formation of the HAGBs. For ribbon A, a (100) cleave was taken, which bisected the starting point of the HAGB [Fig. 2(a)]. For ribbon B, (100) and (001) cleaves were taken in the region just prior to the onset of the HAGB [Fig. 2(b)].

Figure 3 shows EBSD images from regions 1 and 2 on the (001) planes from ribbon A at the locations indicated. The insets show FSD (forward scatter detector) images of the same regions. The growth direction is from right to left in the images. In sample A1 (right), a low angle grain boundary is observed, extending in the direction of the growth axis, with angular mismatches of 1.6°–2.4°. The EBSD signature extending from the center to the top left corner is due to the surface morphology left behind after cleavage and exfoliation of a thin surface layer, as can be seen in the FSD image, rather than any defect structure within the bulk.

In sample A2 (left), taken from a region further down the growth axis, the EBSD image focuses on the region immediately preceding the location of the appearance of a new, polycrystalline grain. That grain became detached from the sample during cleaving, leaving a depressed region that results in the black region in the EBSD image, where no electron diffraction pattern was obtained. This topography change is also visible in the FSD image. The red lines drawn in the figure show where the misorientation across the boundary is measured. Measurements of the degree of misorientation across the boundary approaching this point show the misorientation increasing. At ~4°, the increased strain results in the formation of another grain, relieving local stress and producing a polycrystalline structure in the crystal.

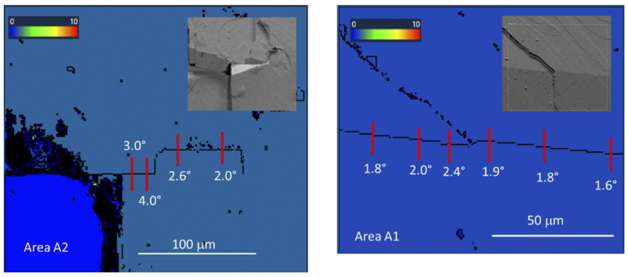

FIG. 3. Ribbon A EBSD average orientation spread maps from areas A1 and A2. The images were taken on the (100) plane, and the colors are related to the value of the orientation spread in each region. The numbers represent the cumulative misorientation across the boundaries. Note that these figures are rotated 90° clockwise from Fig. 2 and the growth direction is from right to left. Insets show the FSD images from the corresponding areas.

Further study of LAGBs was performed on samples from ribbon B, where natural cleavages on the (100) and (001) planes produced accessible surfaces to allow examination of the LAGB in three dimensions. Figure 4 shows EBSD imaging on three of the cleavage faces from sample B1 in Fig. 2. The face in red in Fig. 4 is the (001) face, a cross-sectional surface running ~14° to the pull direction, and the green face is an internal (100) plane, running parallel to the pull direction. Both are perpendicular to the (010) principal face of the ribbon surface, which is shown in the blue EBSD image on the left. We observe the EBSD signatures on the (001) and (100) planes from LAGBs associated with defect planes propagating parallel to the (010) surface. Because this defect zone is parallel to this surface, no corresponding boundaries or defects are observed on the principal face. The measured misorientations at various locations on the (001) and (100) faces are indicated, showing that the misorientation along the LAGB is less than 1°.

Planar grain boundaries on the (−201) surface have been shown by Nakai *et al.*[19] to result from screw dislocations aligning on [102]. However, we have not seen a description of a similar planar grain boundary on the (010) surface. Further studies were undertaken to explore the nature of this grain boundary more fully. The EBSD

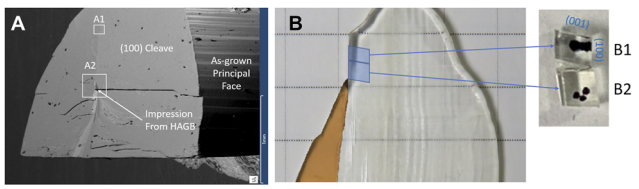

FIG. 2. SEM image of the (010) principal face on ribbon A [(a), left], showing the onset of the HAGB. Optical image of the principle face of ribbon B [(b), right], showing the locations of sample B2 and the location of the HAGB (highlighted).

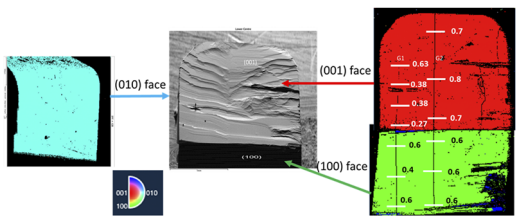

FIG. 4. SEM image (center) of a parallelepiped from sample B2 showing the remaining topography on the (001) face, which has been ion-milled. EBSD IPF images (right) from the (001) and (100) faces of the sample parallelepiped, enabling tracking of the LAGB within the 3D structure. EBSD IPF image (left) from the (010) principal face.

results from samples A and B indicate that the HAGBs appeared in regions containing LAGBs. What is unique in this analysis is the planar nature of the LAGBs, which have been found to be parallel to the principal growth plane for millimeters prior to the consequent HAGB formation. This makes them nearly undetectable through analysis of the principal surface and explains the formation of HAGB in this material without any visual precursors. This also implies that high quality material can exist on either side of the LAGB over mm or larger scales.

We performed ECCI and CL on the same LAGBs to further investigate their structure and potential device impact. LAGBs have been demonstrated to cause increased scattering of majority carriers in Ga_2O_3,[11] but limited work has been carried out confirming the expected impact on minority carrier properties. Figure 5 (top) shows ECCI and CL images, at higher magnification, from the same location along the LAGB on the (001) face observed with EBSD. We see, as expected, regions of structural disturbance, indicated as a bright line along the LAGB in the ECCI image, and a correlated region of increased non-radiative recombination, indicated by the darker line in the CL image. This has been replicated at multiple locations and is consistent with the understanding of the LAGBs as formed by arrays of dislocations.[20] In CL, this dark line indicates decreased intensity in the integrated room temperature emission, which includes both UV (peak at 3.1 eV) and near-IR/visible (peak at 1.8 eV) luminescence. Similar behavior was observed along the full length of the LAGB. Additional variation in the CL image is primarily associated with topography or secondary electron variations, most likely associated with variations in channeling. This is observed as well in the left to right variations of intensity in the ECCI image and is consistent with misorientation across the LAGB.

In the lower part of Fig. 5 we present higher resolution ECCI images taken from a location along the LAGB on both the (001) and the (100) faces. Using the same magnification and channeling conditions, we see the defect present as a bright linear feature on the (001) face and then observe resolved individual dislocation cores on the (100) face. This is consistent with the model of a planar defect arising from strain during growth that causes deformation and insertion of additional lattice planes resulting in dislocations that terminate on the cleaved (100) surface. This is shown in the schematic at the right side in Fig. 5. The appearance of two rows of these bright spots in the ECCI image could be explained by the formation of partial dislocations, reducing local strain energy as the dislocations approach the exposed surface. Further ECCI and high-resolution TEM studies will be required to fully characterize these dislocation cores.

In summary, multimodal characterization has been performed on several ribbons of Ga_2O_3, with the goal of observing the nature and propagation of extended defects during EFG growth. EBSD revealed the presence of LAGBs in the bulk crystals. A LAGB with an increasing degree of misorientation was observed in a region immediately adjacent to the initiation of a HAGB polycrystalline region. Correlated EBSD, ECCI, and CL of an LAGB propagating parallel to the principal face showed enhanced defect contrast consistent with a network of dislocations and increased nonradiative recombination resulting in decreased integrated luminescence intensity.

The work shows the key role of LAGBs in both relieving local strain and potentially seeding the formation of polycrystalline regions in EFG Ga_2O_3. Since LAGBs are able to form parallel to the (010) principal face and propagate millimeters or more before the formation of HAGBs, this highlights the importance of seed quality and early growth parameters aimed at minimizing the formation of dislocation networks in the bulk grown material. It also means that in the absence of HAGB formation these defects can be difficult to detect, as good quality material can exist on either side of the defect. By combining EBSD, ECCI, and CL, we have demonstrated the potential of these techniques to provide insight both into bulk material synthesis and for future

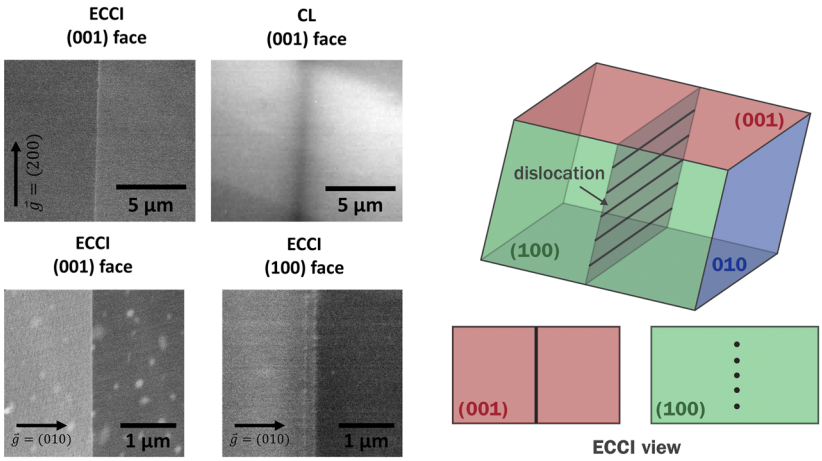

FIG. 5. Top: Correlated ECCI (left) and CL imaging (right) at a location identified on the (001) cross-sectional face of ribbon B, perpendicular to the [001] direction. Bottom: Higher resolution ECCI images of the LAGB on both the (001) and (100) faces. A continuous bright linear feature in ECCI is observed along the LAGB on the (001) face, while terminations of the dislocation cores are resolved on the (100) face. The scattered bright features are due to extrinsic surface contamination. The schematic at the right side shows the nature of the defect formation, propagation, and observation.

studies of epitaxial growth and defect propagation from substrates into active layers.

We thank Bill McMahon for helpful discussions on dislocation properties and for comments on the article. This work was authored by the National Renewable Energy Laboratory (NREL), operated by the Alliance for Sustainable Energy, LLC, for the U.S. Department of Energy (DOE), under Contract No. DE-AC36-08GO28308. The funding was provided by the Office of Energy Efficiency and Renewable Energy (EERE) Advanced Manufacturing Office. The TESCAN Amber S8252G SEM was acquired through the support of the National Science Foundation (Grant No. DMR-1828454). The views expressed in the article do not necessarily represent the views of the DOE or the U.S. Government.

AUTHOR DECLARATIONS

Conflict of Interest

The authors have no conflicts to disclose.

Author Contributions

D.H. and D.J. led the crystal growth efforts and contributed to the conceptualization, writing and review of the research. H.M. performed the EBSD characterization and contributed to the conceptualization, writing and review of the research. J.S.M. performed the ECCI characterization and contributed to the conceptualization, writing and review of the work. H.G. performed the CL characterization and contributed to the writing and review. A.Z. and N.M.H. contributed to the conceptualization, writing and review of the research.

Drew Haven: Conceptualization (equal); Formal analysis (equal); Investigation (equal); Writing – original draft (equal). **Helio Moutinho**: Conceptualization (equal); Data curation (equal); Formal analysis (equal); Investigation (equal); Writing – original draft (equal). **John S. Mangum**: Conceptualization (equal); Data curation (equal); Formal analysis (equal); Investigation (equal); Writing – original draft (equal). **Harvey Guthrey**: Data curation (equal); Formal analysis (equal); Investigation (equal); Writing – original draft (equal). **David Joyce**: Conceptualization (equal); Data curation (equal); Formal analysis (equal); Investigation (equal); Writing – original draft (equal); Writing – review & editing (equal). **Andriy Zakutayev**: Conceptualization (equal); Writing – review & editing (equal). **Nancy M. Haegel**: Conceptualization (equal); Formal analysis (equal); Writing – original draft (equal); Writing – review & editing (equal).

DATA AVAILABILITY

The data that support the findings of this study are available from the corresponding author upon reasonable request.

REFERENCES

[1] A. J. Green, J. Speck, G. Xing, P. Moens, F. Allerstam, K. Gumaelius, T. Neyer, A. Arias-Purdue, V. Mehrotra, A. Kuramata, K. Sasaki, S. Watanabe, K. Koshi, J. Blevins, O. Bierwagen, S. Krishnamoorthy, K. Leedy, A. R. Arehart, A. T. Neal, S. Mou, S. A. Ringel, A. Kumar, A. Sharma, K. Ghosh, U. Singisetti, W. Li, K. Chabak, K. Liddy, A. Islam, S. Rajan, S. Graham, S. Choi, Z. Cheng, and M. Higashiwaki, APL Mater. **10**(2), 029201 (2022).
[2] K. N. Heinselman, D. Haven, A. Zakutayev, and S. B. Reese, Cryst. Growth Des. **22**(8), 4854–4863 (2022).
[3] M. D. McCluskey, J. Appl. Phys. **127**(10), 101101 (2020).
[4] J. Lee, S. Ganguli, A. K. Roy, and S. C. Badescu, J. Chem. Phys. **150**(17), 174706 (2019).
[5] O. Ueda, M. Kasu, and H. Yamaguchi, Jpn. J. Appl. Phys. **61**(5), 050101 (2022).
[6] K. Z. Baba-Kishi and D. J. Dingley, Scanning **11**(6), 305–312 (1989).
[7] D. J. Dingley and V. Randle, J. Mater. Sci. **27**(17), 4545–4566 (1992).
[8] D. Stojakovic, Process. Appl. Ceram. **6**(1), 1–13 (2012).
[9] A. J. Wilkinson, G. Meaden, and D. J. Dingley, Mater. Sci. Technol. **22**(11), 1271–1278 (2006).
[10] J. Jesenovec, J. Varley, S. E. Karcher, and J. S. McCloy, J. Appl. Phys. **129**(22), 225702 (2021).
[11] C. Golz, Z. Galazka, J. Lähnemann, V. Hortelano, F. Hatami, W. T. Masselink, and O. Bierwagen, Phys. Rev. Mater. **3**(12), 124604 (2019).
[12] Y. Oshima, K. Kawara, T. Oshima, and T. Shinohe, Jpn. J. Appl. Phys. **59**(11), 115501 (2020).
[13] J. I. Deitz, S. D. Carnevale, S. A. Ringel, D. W. McComb, and T. J. Grassman, J. Visualized Exp. **101**, e52745 (2015).
[14] S. D. Carnevale, J. I. Deitz, J. A. Carlin, Y. N. Picard, M. D. Graef, S. A. Ringel, and T. J. Grassman, Appl. Phys. Lett. **104**(23), 232111 (2014).
[15] G. Naresh-Kumar, D. Thomson, M. Nouf-Allehiani, J. Bruckbauer, P. R. Edwards, B. Hourahine, R. W. Martin, and C. Trager-Cowan, Mater. Sci. Semicond. Process. **47**, 44–50 (2016).
[16] F. Ram, Z. Li, S. Zaefferer, S. M. Hafez Haghighat, Z. Zhu, D. Raabe, and R. C. Reed, Acta Mater. **109**, 151–161 (2016).
[17] Y. N. Picard, Microsc. Microanal. **24**(S1), 630–631 (2018).
[18] B. Hauer, C. E. Marvinney, M. Lewin, N. A. Mahadik, J. K. Hite, N. Bassim, A. J. Giles, R. E. Stahlbush, J. D. Caldwell, and T. Taubner, Adv. Funct. Mater. **30**(10), 1907357 (2020).
[19] K. Nakai, T. Nagai, K. Noami, and T. Futagi, Jpn. J. Appl. Phys. **54**(5), 051103 (2015).
[20] D. Hull and D. J. Bacon, *Introduction to Dislocations*, 5th ed. (Elsevier, 2011).